

Rijksuniversiteit Groningen

Faculteit der Wiskunde en Natuurwetenschappen

A Technique to study spin transport at the nanoscale

NS 190 PAPER BY: Morten Bakker

Supervisor: Dr. Tamalika Banerjee

Date: 1 June 2009



**rijksuniversiteit
 groningen**

Abstract

This paper discusses the evolution of a unique microscopic and spectroscopic tool, over the past two decades, from probing metal-semiconductor interfaces, into a versatile technique for nanometer scale characterization exploiting a wide range of materials and their interfaces. The technique known as Ballistic Electron (Holes) Emission Microscopy (BE(H)EM) uses ballistic transport of hot carriers to study the structural and electronic properties and their correlation with excellent resolution. The basic idea behind the technique, aspects of BEEM experiments and theory and their recent progress in the past few years has been discussed.

The important mechanisms that contribute to the BEEM current and its spectral shape have been discussed with the help of theoretical models. The importance of studying spin-dependent transport of hot carriers (on energy scales $\sim 1-5$ eV above E_F) is driven by the emergence of spintronics and is of great interest for the design of spintronic devices. With the rapid downsizing of the devices, a better understanding of the fundamental physics concerning spin transport of hot carriers at the nanoscale is necessary. In this respect, BEEM and its related techniques are capable of quantitatively studying this in a non-destructive manner with an excellent resolution at the nanoscale. Several examples how these techniques revealed new physical aspects behind spin-dependent transport and scattering processes have been presented.

BEEM also presents ways of imaging magnetic structures and interfaces with resolutions ~ 10 nm and holds promise of doing this with even smaller resolution.

Contents

Introduction.....	4
1. Ballistic electron emission microscopy and related techniques.....	5
1.1. Principle.....	5
1.2. Models describing the collector current.....	7
1.3 Near threshold collector current.....	10
1.4 Spectroscopy measurements.....	12
1.5 Imaging.....	12
2 Emergence of spin electronics.....	14
3 Ballistic electron magnetic microscopy and related techniques.....	17
3.1 Principle	17
3.2 Samples and experimental setup.....	18
4 Hot Carrier transport.....	20
4.1 Hot electrons	20
4.2 Hot holes	24
5 Nanoscale magnetic imaging.....	26
Conclusions.....	28
Acknowledgments.....	28
References	29

Introduction

Transport of electrons and holes is of great interest for the design of electronic devices. Ballistic Electron Emission Microscopy (BE(H)EM) and Ballistic Hole Emission Microscopy (BHEM) are unique research tools, as they can study at the nanoscale in a non-destructive manner properties of propagating non-equilibrium electrons or holes and their scattering mechanisms. They can simultaneously study both buried interfaces and surface morphology in a quantitative way.

The discovery of the 'Giant Magneto Resistance' (GMR) in 1988 by Fert *et al.* triggered the emergence of spintronics. Fundamental understanding and application of the magneto current transport properties at the Fermi level and above it (hot carriers) in magnetic multilayer systems became essential.

The relatively new Ballistic Electron Magnetic Microscopy (BEMM) and Ballistic Hole Magnetic Microscopy (BHMM) techniques are based on BEEM and BHEM and are capable of meeting these demands. They are the only techniques capable of measuring properties of spin-dependent transmission of electrons and holes $\sim 1-5$ eV above or below the Fermi level. It is unique as it is capable of retrieving quantitative information in a non-destructive manner about spin-dependent scattering processes in materials and at interfaces. Using these unique techniques not earlier examined physical processes of hot electron and hole scattering can be studied.

Also it is an excellent tool to examine nanoscale magnetic structures and study the behaviour of magnetic domains and interfaces.

1. Ballistic electron emission microscopy and related techniques

1.1 Principle

Ballistic Electron Emission Microscopy (BEEM) was first demonstrated by LD Bell and WJ Kaiser in 1988 [1]. In their pioneering work they used BEEM to image the subsurface structure of Au/Si(100) and Au/GaAs(100) systems and used spectroscopy to measure the Schottky barrier heights (SBH). Ballistic hole emission microscopy (BHEM) was demonstrated a few years later by Hecht *et al.* [2], who studied hole transmission through Au/Si(100) and Au/GaAs(100) interfaces and used this to probe the valence-band structure of the subsurface semiconductor heterostructures. A good review about the early work with BEEM and BHEM is provided by [3].

The experimental setup of the BEEM and related techniques is schematically shown in Fig 1. By applying a tip voltage V_T between a scanning tunnelling microscope (STM) tip and the base layer, a non-equilibrium (hot) carrier current I_T is injected into the base layer, typically a thin metal film. Samples consist of a single metal film or a metal thin film stack grown on a semiconductor (or heterostructure) substrate. The figure shows the simple example of a single metal layer deposited on a semiconductor substrate. In addition to the usual STM image of the sample surface, a contact at the back of the semiconductor substrate is used to collect the hot carrier current I_C that is transmitted through the metal film(s) into the semiconductor substrate.

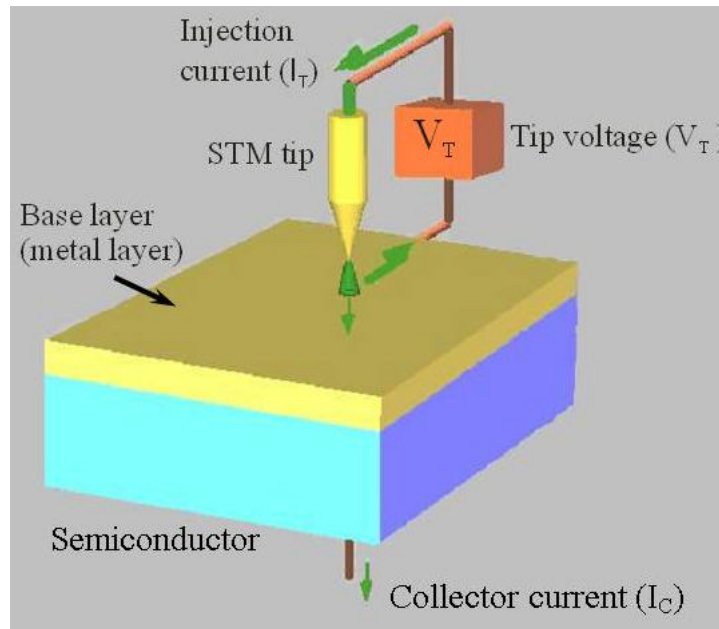


Fig 1. Experimental setup used for BEEM and related techniques. A STM-tip with voltage V_T injects a current I_T into the base layer (metal film). A current I_C is collected at the back of the semiconductor substrate.

Depending on the tip voltage V_T hot electrons (in the case of BEEM experiments) or hot holes (BHEM) are injected. The experiment can be operated in normal mode or reversed mode. Schematic band diagrams of BEEM/BHEM in normal/reversed mode experiments on a metal film deposited on a n/p-doped semiconductor substrate are shown in Fig 2.

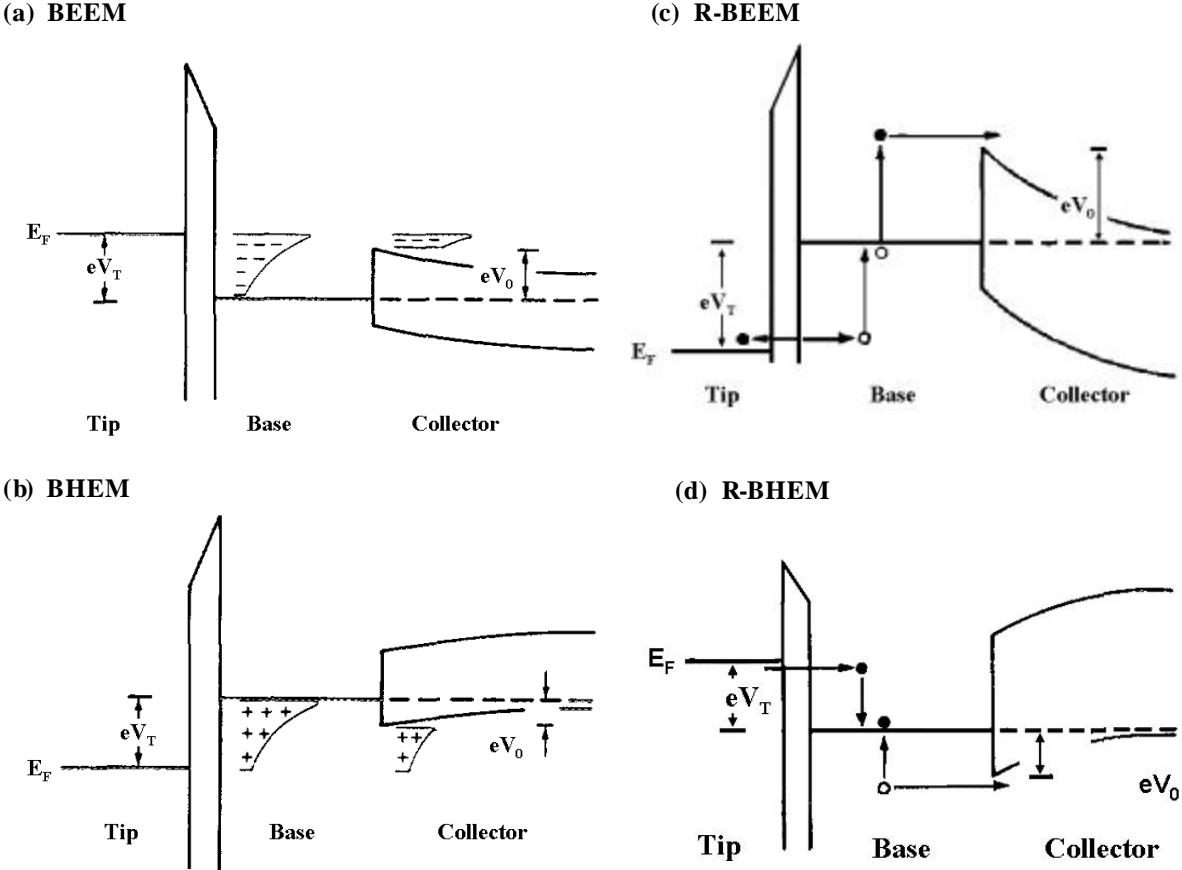


Fig 2. Schematic energy band diagrams for BEEM and BHEM operating in normal and in reversed mode.

In normal mode hot electrons (Fig 2(a)) or hot holes (Fig 2(b)) are injected from a STM-tip, through a vacuum barrier, into unoccupied states in the base (typically a thin metal layer). After transmitting through the base layer, hot carriers that have high enough energy to pass the Schottky barrier height eV_0 and conserve momentum parallel to the interface are able to transfer the metal-semiconductor interface and are collected in the n-type (for electrons) or p-type (holes) semiconductor, resulting in a collector current I_C .

In 1994 the first experiments using BEEM operating in reverse mode were performed by Davies and Craighead [4]. The effect of the image potential on the Schottky barrier reduction by applying a positive voltage was studied in Au/n-Si. Due to a reduction in energy dependent back scattering of electrons the collector current increased.

In BEEM experiments operated in reverse mode (R-BEEM) a positive voltage V_T is applied, see Fig 2(c). High energetic holes that are created by tunnelling electrons from the base to the tip, create electron-hole pairs by scattering. Hot electrons created that meet

energetic and momentum conservation are able to be collected in the n-type semiconductor.

In BHEM experiments operated in reverse mode (R-BHEM) a negative voltage V_T is applied, see Fig 2(d). Electrons that tunnel from the tip into the sample can create electron-hole pairs by scattering. Holes can then be collected in the p-type semiconductor.

1.2 Models describing the collector current

Several models have been developed to describe the collector current I_C as function of the applied tip voltage V_T . BEEM operated in normal mode for a metal thin film on top of a n-type semiconductor will be discussed as it is fairly straightforward and exemplarily for the various mechanisms that have to be considered. The two most common used models are the Bell-Kaiser (BK) model [5] and the Ludeke-Prietsch (LP) model [6]. They take into account four important mechanisms:

1) Tunnelling from the tip into the sample. The resulting angular and energetic distribution of electrons in the metal film can be described using planar tunnelling theory [7]:

$$I_T = \frac{eA}{4\pi^3\hbar} \int_0^\infty dE_x \times D(E_x, V_T) \iint (f(E) - f(E + eV_T)) dk_t^2 \quad (1)$$

E_x (E_t)/ k_x (k_t) is the energy/ momentum of electrons perpendicular (parallel) to the metal surface. A is the total surface electrons are injected into. $D(E_x, V_T)$ is the transmission factor for tunnelling, $f(E)$, $f(E+eV_T)$ are the Fermi-Dirac functions of the tip. For a rectangular barrier of average height $f_0(V_T)$ and width d , the transmission factor is given by [7]:

$$D(E_x, V_T) = \exp(-Cd(\mathbf{j}_0(V_T) - E_x + E_F)) \quad (2)$$

Here E_F is the Fermi level in the tip and C a certain constant. For a STM-tip with radius $\sim 10 \text{ \AA}$, equation (1) can be integrated and gives for $T=0 \text{ K}$ [8]:

$$I_T = \frac{eA}{\hbar(2\pi^3 d)^2} (\mathbf{j} \exp(-Cd\mathbf{j}^{1/2}) - (\mathbf{j} + eV_T) \exp(-Cd(\mathbf{j} + eV_T)^{1/2})) \quad (3)$$

Here $f = (f_T - eV_T/2)$, with f_T the metal work function of the tip. The number of electrons $\frac{dI_T}{dE}$ that are injected with an energy E is schematically shown in Fig 3.

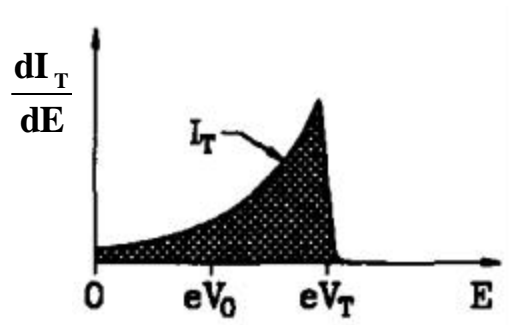


Fig 3. Distribution of tunnelling current by applying a tip voltage V_T . The Schottky barrier height is denoted with V_0 . Total injected current is I_T . The figure is reproduced from [9].

2) The transport through the base layer. The transmittance $T(E)$ of the number of electrons that are transmitted through the base layer shows an exponential decay:

$$T(E) = \exp(-d/\lambda(E)), \quad (4)$$

where d the thickness of the base layer and $\lambda(E)$ the energy dependent attenuation length of the electrons. $\lambda(E)$ is defined as the distance where the current has dropped by $1/e$. It is mainly determined by electron-electron scattering, but also by scattering due to phonons and impurities and other interesting physical effects like energy dependent propagation velocity. The typical dependence of $T(E)$ on the energy E of hot electrons is show in Fig 4. For small variations in energy $\lambda(E)$ is often assumed to be constant.

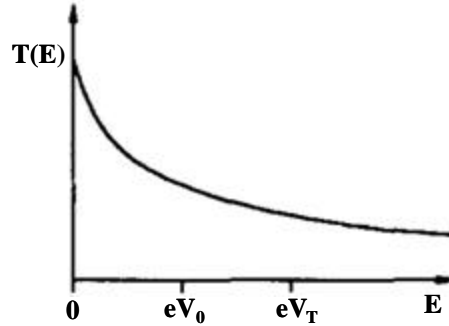


Fig 4. Transmission through metal film with thickness d . Figure is reproduced from [9]

3) The transmission from the metal to the semiconductor. During this process energy and momentum parallel to the interface is conserved. Due to a much smaller electron mass in the semiconductor a electron refraction effect occurs at the interface. The injected electrons in the metal have a maximum kinetic energy $E = eV_T + E_F$, after passing the Schottky barrier height the electrons have a maximum kinetic energy $E = eV_T - eV_0$. As the transverse momentum $p_t = \sqrt{2mE} \sin(\theta)$, with θ the angle of incidence, is conserved along the interface, it follows that the critical angle θ_c at which the electrons can still propagate from the metal into semiconductor is given by [5]:

$$\sin^2(\theta_c) = \frac{m^*}{m_0} \frac{eV_T - eV_0}{eV_T + E_F}, \quad (5)$$

Where m^* is the effective electron mass in the semiconductor and m_0 the (free electron) mass in the metal. The result of this refractive effect is that electrons are only collected in a cone with angle θ_c , electrons with an angle of incidence $> \theta_c$ are reflected at the interface. This is clearly illustrated in Fig 5. Due to large electron mass mismatch (in GaAs for example $m^* = 0.067 m_0$.) θ_c is often only a few degrees, resulting in a collection cone < 10 nm and therefore a good lateral resolution.

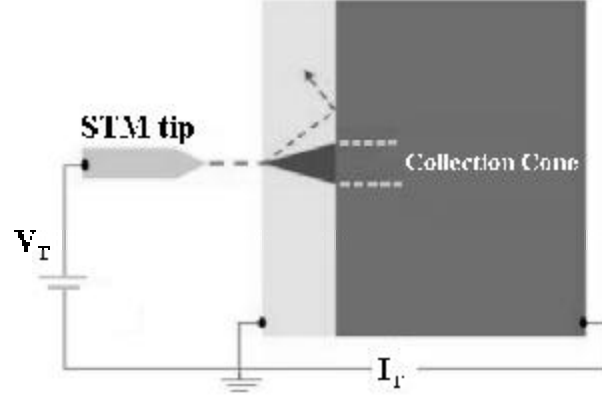


Fig 5. Schematic view of a BEEM experiment, illustrating how electrons are only collected in a collection cone.

In the LP model it is assumed that transmission for electrons having sufficient energy $E > eV_0$ and satisfying the momentum conservation is a step function.

In the BK model the quantum mechanical transmission (QMT) factor for an abrupt interface is taken into account, given by [11]:

$$C(E, k_t^m) = \frac{4k_x^m k_x^s}{m_0 m_x^* (k_x^m / m_0 + k_x^s / m_x^*)^2} \quad (6)$$

Here $k_{x(t)}^{m(s)}$ denotes the momentum component perpendicular (parallel) to the interface in the metal (semiconductor). m_x^* is the electron effective mass in the semiconductor parallel to the interface, m_0 is the (free) electron mass in the metal. The transmission for normal ($k_t^m = 0$) and non-normal ($k_t^m \neq 0$) incidence is schematically shown in Fig 6.

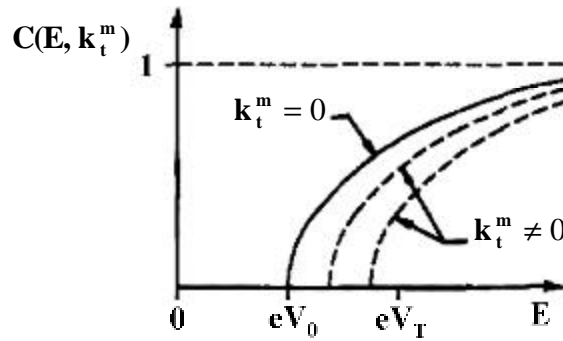


Fig 6. Transmission across interface for normal and non normal incidence.

4) Transmission through the semiconductor. It is assumed that the transmission T^{SC} does not affect the shape of the energy distribution of the collector current.

The resulting final energetic distribution of the collector current $\frac{dI_C}{dE}$ for the LP model is shown in Fig 7. For the BK model this looks quite similar.

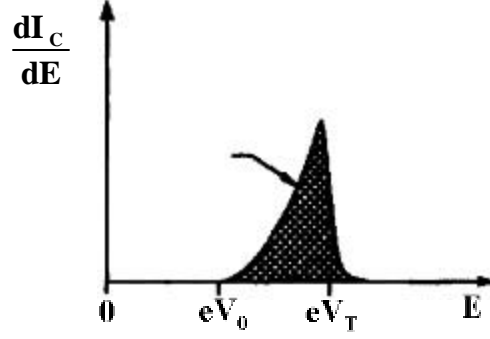


Fig 7. Final energetic distribution of the collector current I_C according to the LP model.

The exact final expression for the collector current is finally given by:

$$I_C = \frac{eA}{4\pi^3 \hbar} \int_0^\infty dE_x \times D(E_x, V_T) \iint T^{SC} C(E_x, E_t) T(E_x, E_t, k_t) (f(E_x + E_t) - f(E_x + E_t + eV_T)) dk_t^2 \quad (7)$$

I_C is thus only dependent on the available tip states with transverse momentum k_t and the probability of an electron with energy E_x perpendicular to the surface and energy E_t parallel to the surface to transmit from tip to sample (D), transfer through the metal layer (T), cross the metal-semiconductor interface (C) and transfer through the semiconductor (T^{SC}). The amount of collected current is typically <10% of the total tunnelling current.

1.3 Near threshold collector current

For voltages slightly above the threshold voltage V_0 , the collector current can be modelled using the LP or BK model. For higher voltage, typically $V \sim 200$ meV above V_0 , deviations arise, mainly due to a voltage-dependent energetic distribution of the tunnelling current, carrier scattering in the metal over layer as well as carrier scattering and impact ionization in the semiconductor substrate. A good overview of these processes is provided by [13].

In a typical experiment a constant current is injected into the base layer. The solid angle under which electrons are accepted follows from the critical angle θ_C and is given by:

$$\Omega = \frac{\mathbf{p} \cdot \mathbf{m}^*}{2 m_0} \frac{V_T - V_0}{V_T + E_F} \quad (8)$$

Assuming the attenuation length $\lambda(E)$ is constant and transmission across the interface to be a step function, the change in collector current ΔI_C by increasing the voltage with ΔV_T is given by the BK model to be:

$$\Delta I_C = C I_C \frac{\Delta V_T}{V_T} \Omega \quad (9)$$

Here C is a constant. Note the factor $\frac{\Delta V_T}{V_T}$, as there is a constant injection current and applying a higher voltage therefore only increases the relative amount of high energy electrons with $\frac{\Delta V_T}{V_T}$.

By integrating from V_0 to V_T , it follows that according to the BK model the near threshold current I_c in the low temperature limit varies:

$$I_C \propto (V_T - V_0)^2 \quad (10)$$

By taking the QMT into account, the transmission probability near the threshold increases with $C(E, k_x^m) \propto (V_T - V_0)^{1/2}$. This results into, according to the LP model:

$$I_C \propto (V_T - V_0)^{5/2}, \quad (11)$$

for voltages just above threshold.

Which model is most preferable to use is however strongly dependent on the band structure of the semiconductor at the interface. Some examples of projections of the constant energy surface onto the interface are shown in Fig 8 for some common used semiconductors. Depending on the semiconductor and its orientation, the electrons must have a large transverse momentum to phase match (for example Si(111)) or must be near normal incidence (for example GaAs(100)) to be transmitted. In case of Si(100) it is more complicated as electrons with both large as small transverse momenta are transmitted.

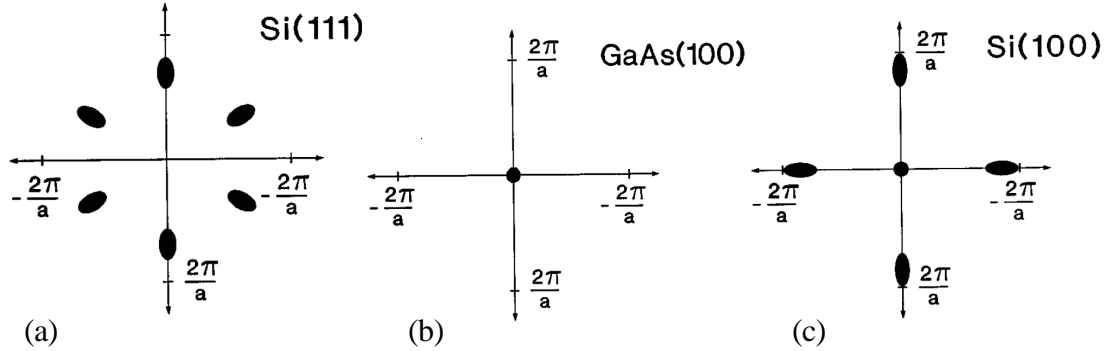


Fig 8. Projection of the constant energy surfaces onto the interface plane for (a) Si(111), (b) GaAs(100) and (c) Si(100). Figure is reproduced from [14].

In case the allowed k values the electrons can transfer into are zone centred, the additional considerations about the quantum mechanical transmission becomes negligible, and the collector current can be easily fitted using the BK model. If however non zone-centred k space values become important, the LP model gives better results. However, this is not always the case. It is often demonstrated that for samples that require extra lateral momentum for the electrons to match the band structure of the semiconductor, the current is reduced, but due to experimental error the subtle difference between the power 2 and power 5/2 dependence can often be negligibly small. Sometimes a different model is used, than based on the used semiconductor seems justifiable, for example [16].

Using the BEEM and BHEM technique, spectroscopic and imaging studies can be performed. It has proven to be a very versatile tool to characterize simultaneously structural and electronic properties of metallic and semiconducting materials and their interfaces at the nanometer-scale. It is a unique technique as it can be used to simultaneously study surfaces but also buried interfaces in a non-destructive manner. Some typical experimental results will be briefly discussed.

1.4 Spectroscopy measurements

Using the BEEM and BHEM techniques, spectroscopic studies can be done by fixing the STM-tip on one certain position. The highest emphasis in the early work was using BEEM to measure Schottky barrier heights this way, as this was more accurate than using photo emission techniques. By measuring BEEM spectra this could be done with high accuracy although the accuracy was limited by surface topology and tip contaminations. Fits using the BK or LP model give slightly different results for the SBH, but this difference is typically only of the order ~ 0.02 eV [6]. Some excellent results are shown in Fig 9, where Ludeke *et al.* measured the SBH of several different metals deposited on n-GaP(110) with great precision using the LP model.

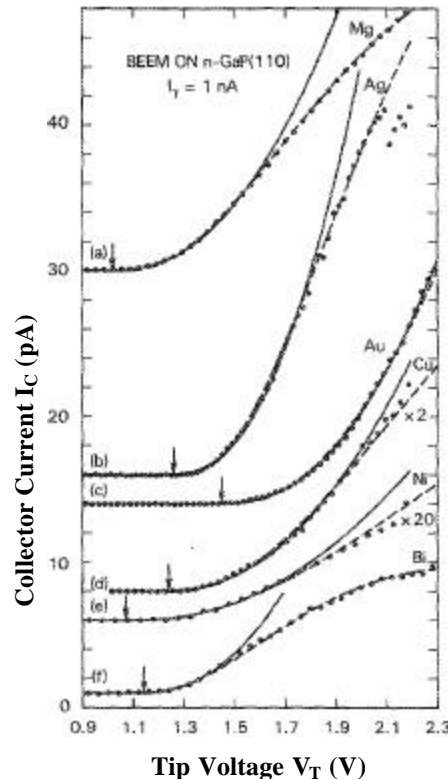


Fig 9. BEEM spectra measured for several metal layers deposited on n-GaP(110). Solid lines are fits using the LP model. Dashed lines are fits where electron scattering effects in the metal film are also included.

Figure reproduced from [6].

1.5 Imaging

As discussed previously, due to transverse momentum only hot electrons or holes with an angle of incidence smaller than the critical acceptance angle θ_c (see equation 5 and Fig 5) are collected. Since hot carriers initially tunnelling into the base are highly focused in the forward direction, the acceptance angle (typically only a few degrees) acts as a filter to only collect ballistic electrons or holes. This results in a very high spatial resolution. Siringhaus *et al.* even demonstrated atomic scale resolution on the order of 1.5 \AA [16]. They imaged periodic surface structures at atomic resolution using BEEM on $\text{CoSi}_2/\text{n-Si}(100)$, see Fig 10. They explained the surface contrast by atomic scale variations of the energy distribution of the injected carriers induced by variations of the tunnelling barrier.

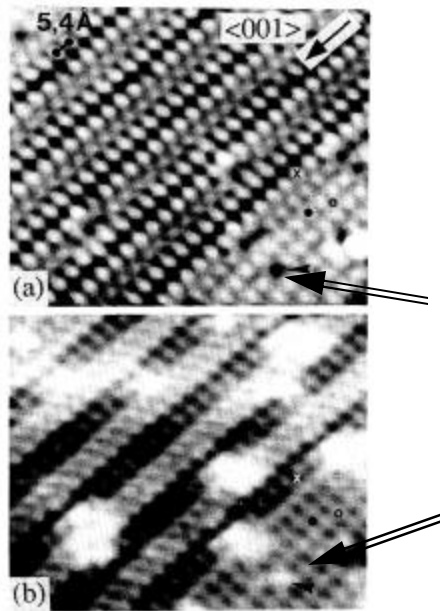


Fig 10. (a) STM topographic image) and (b) simultaneously recorded forward BEEM image on the Si-rich n-Si(100) CoSi₂ surface ($V_T = -1.5$ V, $I_T = 3$ nA, film thickness $d = 38$ Å). An atomic scale resolution is demonstrated. A dislocation in top image (see arrow top figure) leads to an increased BEEM current (see arrow bottom figure). Figure is reproduced from [16].

2 Emergence of spin electronics

The simultaneous but independent discovery of giant magneto resistance (GMR) in 1988 by Fert *et al.* [17] and Grünberg *et al.* [18] marked the emergence of the importance of spin electronics. The group of Fert discovered a giant magnetoresistance in (001)Fe/(001)Cr super lattices when there is an anti-parallel coupling for zero field. The resistance dropped considerably when applying a magnetic field in the plane of the layers, which magnetically aligns the two layers. The founding results are shown in Fig 11. The group of Grünberg discovered a similar phenomenon but for Fe/Cr/Fe trilayers.

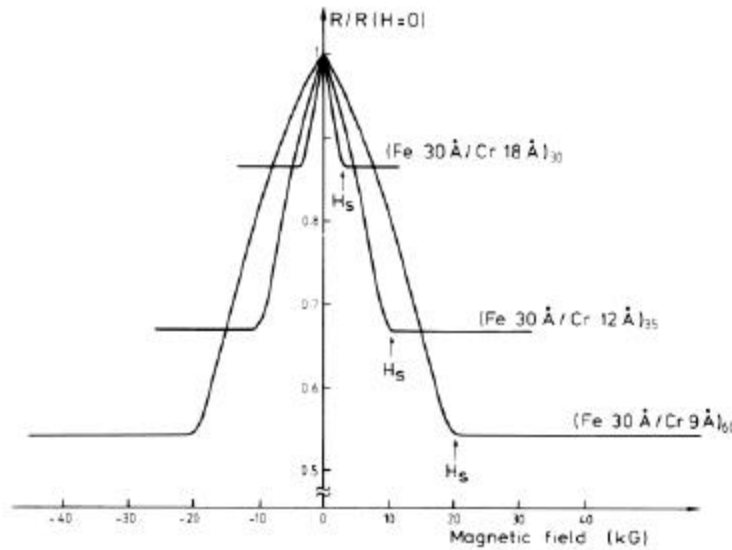


Fig 11. Magneto-resistance of three Fe/Cr superlattices at $T=4.2$ K. The current and the applied field are in the plane of the layers. Figure is reproduced from [17].

In ferromagnetic transition metals, because of exchange splitting, a large asymmetry of the density of states (DOS) of the spin-up and spin-down electrons at E_F exists. An example of such a material is cobalt; the spin-resolved DOS is shown in Fig 12.

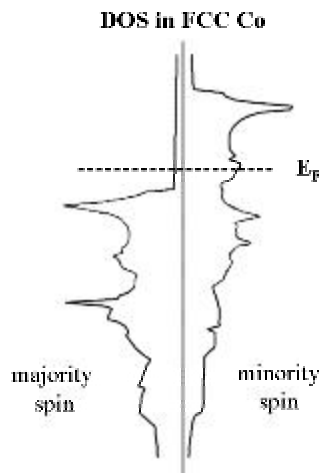


Fig 12. Spin-resolved density of states of face-centered cubic (FCC) Co. A large anisotropy can be seen for electrons around the Fermi level, resulting in an increased scattering probability for hot electrons with minority spin. Figure is reproduced from [21].

According to Fermi's golden rule, the scattering probability of an electron with a certain spin orientation depends on the number of states the electron can decay into, while preserving spin orientation. In a ferromagnetic material, the asymmetry in DOS causes the electrons with one spin orientation to have a larger inelastic scattering probability (minority carriers) than the electrons with an opposite orientation (majority carriers). Thus the difference in inelastic lifetime causes the conduction to be largely dependent on the spin orientation of the charge carriers.

The GMR effect is exploited in a spin valve, where two ferromagnetic layers are separated by a non-magnetic metallic or insulating spacer layer. The schematic working of a spin valve is shown in Fig 13. When the two ferromagnetic layers are magnetized parallel (P), the majority spin electrons (spin anti-parallel to the magnetization) can travel through the sandwich nearly unscattered. Minority spin electrons get strongly scattered. In the case the ferromagnetic layers are magnetized anti-parallel (AP), both spin-up and spin-down electrons undergo equal scattering, giving rise to a higher resistance.

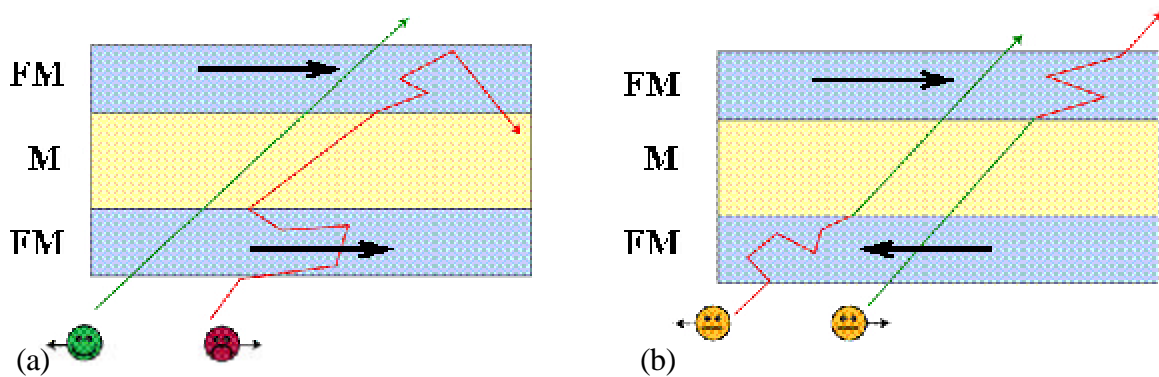


Fig 13. Spin valve consisting of two ferromagnetic layers (FM) and non-magnetic spacer layer (M). (a) When the two ferromagnetic layers are magnetized parallel, the majority (spin-up) electrons can travel through them relatively easy, while minority carriers get scattered. (b) In an anti-parallel alignment both get scattered, resulting in a reduced current. Figure is reproduced from [19].

In classical electronics only charges are used to transport, manipulate or store information. The discovery of the GMR effect opened the way to spin-dependent transport in addition to charge transport, thus opening the field of spintronics. The first applications include read heads for data storage and magnetic sensors. Recently, the GMR effect has also been applied for solid-state magnetic storage. The first Magnetic Random Access Memory (MRAM) was commercialized in 2006, combining properties like non-volatility, infinite endurance and fast random access, that make it a possible candidate to replace all future memory devices [22].

For the application and further development of devices based upon spintronics, it is important to study the properties of spin-dependent transport of hot electrons and holes. The GMR phenomenon occurs for transport around the Fermi-level. Magnetic tunnel junctions can be used to probe the transport of hot carriers above the Fermi-level but is limited by the breakdown voltage of the tunnel barrier (usually 1-1.5 eV) used in such devices. As the work function of metals is typically ~5 eV, photo emission techniques

can only be used to study the transport of hot carriers in this energy range. Electron and hole transport above E_F (hot electrons/holes) has been largely unexplored, but is however quite important as this also happens to be the area where charge carrier devices typically operate.

BEEM is by far the most versatile technique to study spin-dependent hot carrier transport in this energy range and to obtain physical insight into the scattering processes of hot electrons and holes. BEEM (and its associated techniques) exploits spin transport of non-equilibrium carriers in magnetic heterostructures at the nanoscale with a high resolution. The spectroscopy feature allows us to probe spin transport not only at the surface but at buried interfaces as well and gives valuable information regarding the scattering mechanisms operating at these energy scales. As most common understanding on magnetism is based on macroscopic studies, this technique is also a powerful tool to study magnetic domains, interfaces, etc on the nanoscale and broaden our current understanding.

3 **Ballistic electron magnetic microscopy and related techniques**

Ballistic Electron Magnetic Microscopy (BEMM) was introduced as the magnetic counterpart of BEEM. It was firstly demonstrated by Rippard *et al.* in 1999 [20]. They studied magnetic structure in Co/Cu/Co trilayer structures and observed magnetic domains and domain-wall motion with nanometer resolution. Ballistic Hole Magnetic Microscopy (BHMM) was firstly demonstrated by Banerjee *et al.* in 2005 [21]. They studied the hole attenuation length in Co and the hole transmission of a $\text{Ni}_81\text{Fe}_{19}/\text{Au}/\text{Co}$ trilayer which they found is clearly spin-dependent. Magnetic imaging with holes at buried interfaces were also demonstrated with a resolution of 20 nm.

3.1 Principle

BEMM and BHMM are similar to BEEM and BHEM except that it uses a spin valve in the metal layer stack and an external magnetic field is applied. The basic schematic is shown in Fig 14.

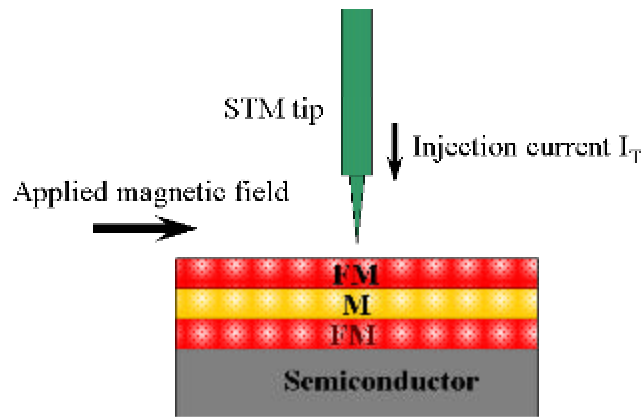


Fig 14. Schematic setup for BEMM and BHMM. It is similar to BEEM, only the current is injected into a spin valve, consisting of two ferromagnetic layers (FM) separated by a non-magnetic (metallic or insulating) spacer layer (M). An external magnetic field is applied parallel to the surface.

The technique relies on the fact that scattering of hot carriers in ferromagnets is spin-dependent, the collector current I_C is therefore high when both layers are magnetically aligned parallel and reduced for anti-parallel alignment. The first ferromagnetic layer effectively acts as a polarizer, while the second layer serves as an analyser.

The schematic energy diagrams for BEMM and BHMM operated in normal and reversed mode are shown in Fig 15.

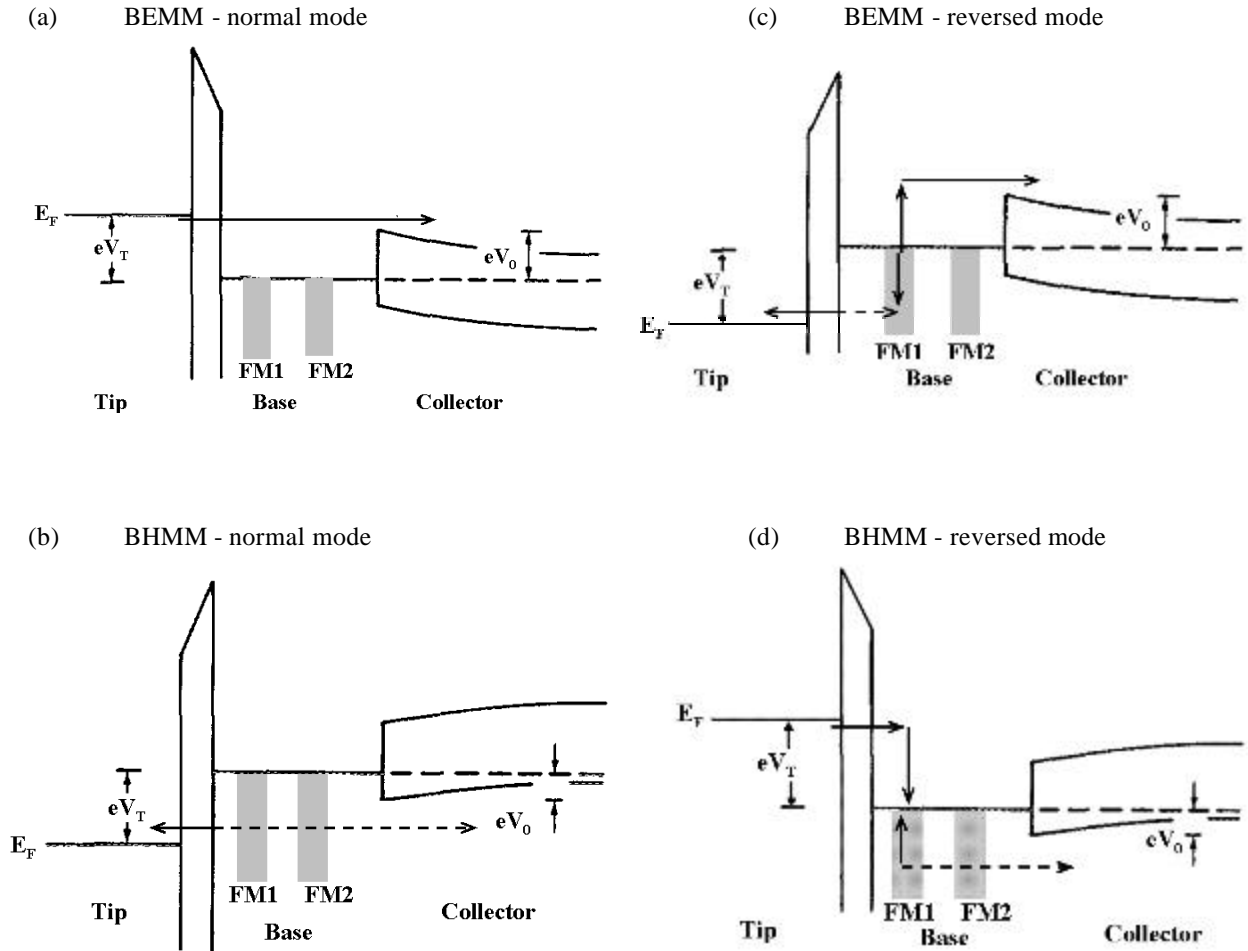


Fig 15. Schematic energy band diagrams for BEMM and BHMM operated in normal and reversed mode. Solid (dashed) lines denote transport of electrons (holes).

A STM-tip is used to inject unpolarized hot electrons or holes into a ferromagnetic thin film stack consisting of ferromagnetic thin films FM1 and FM2 (shown in grey).

The first measurements performed in reverse mode were performed by Banerjee *et al.* in 2005 [23]. They used BHMM in reverse mode to study spin-dependent transmission of excited holes through $\text{Au/Co/Au/Ni}_{81}\text{Fe}_{19}/\text{Au}$ structures. They obtained local hysteresis loops and performed high resolution magnetic imaging. Schematic energy diagrams of BEMM and BHMM operated in reverse mode are shown in Fig 15(c,d). Hot electrons or holes are injected. Inelastic scattering in the magnetic layers creates electron-hole pairs, inducing a spin-dependent electron (Fig 15(c)) or hole (Fig 15(d)) current.

3.2 Samples and experimental setup

Samples are typically fabricated by depositing the desired magnetic thin films on top of a semiconductor surface using molecular-beam epitaxy in a UHV system or by sputtering. The ferromagnetic materials that are typically studied are among others Fe, NiFe and Co, as these ferromagnetic materials possess interesting properties applicable for spin valve

transistors. Noble metals as Au or Cu with long inelastic scattering lengths are used to magnetically decouple the two magnetic thin films.

When the sample has to be transported *ex situ* to the measurement setup, the sample is often terminated to prevent oxidation of the surface. This is typically done using a thin (~3 nm) layer of Au. The measurements are performed using a standard STM-tip, typically PtIr which is electrochemically etched to make it as sharp as possible. The experiments are performed in UHV (base pressure $\sim 10^{-10}$ mbar) and both at room temperature or at low temperatures (4 K).

4 Hot Carrier transport

Several factors influence transport of hot carriers, such as electron-electron scattering, energy and spin-dependent DOS, energy band dependent propagation velocities, spin-polarizing effects at interfaces, etc. To demonstrate the versatility of the described techniques, some examples of measurements performed to examine the properties of hot electron and hole transport will be discussed.

4.1 Hot electrons

Using Equation 5, the attenuation length $\lambda(E)$ in a metal layer with thickness d for non-polarized hot electrons follows the relationship:

$$I = I_0 e^{\frac{-d}{\lambda(E)}} \quad (12)$$

When spin-up and spin-down electrons have different attenuation lengths, as in ferromagnets, but their different contributions cannot be distinguished, it is better to speak about the total effective attenuation length λ_{eff} .

By measuring the collector current using constant injection current for samples with a metal layer of various thickness and tip voltages, the (effective) attenuation length can be easily determined as function of energy using the BEEM technique. An interesting example of such a measurement is performed by Stollenwerk *et al.* [24] on Au/Fe/Si(001) and Au/Fe₈₁C₁₉/Si(001) samples. They performed spectroscopic measurements, fitted using the LP model, see Fig 16(a). The BEEM spectrum of Fe₈₁C₁₉ shows a characteristic development as also seen in Fig 9, however the Fe spectrum shows a second threshold around 1.29 ± 0.04 eV, attributed to the existence of an additional conduction band minimum (CBM) that arises from the bonding of the Fe to the Si.

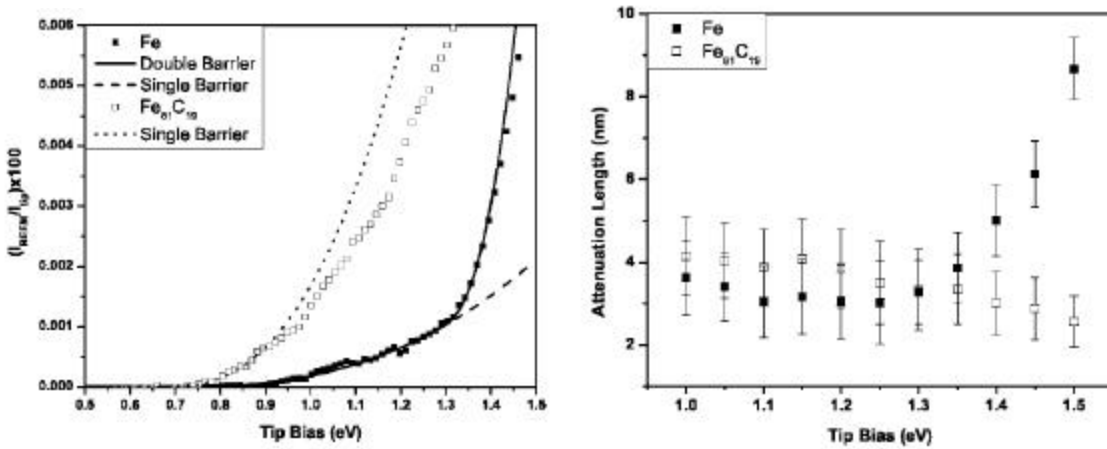


Fig 16. (a) BEEM spectra on Fe₈₁C₁₉ and Fe samples. Fe has a second threshold around ~1.29 V. (b) This also corresponds with an increase in the hot electron effective attenuation length for energies above ~1.25 eV. Figure is reproduced from [24].

The effective attenuation lengths in Fe₈₁C₁₉ and Fe are shown in Fig 16(b). The effective attenuation length in Fe₈₁C₁₉ decreases with increasing energy, as the electron-electron scattering increases. When electron-electron scattering is the dominating factor, it is often

seen in metals that the effective attenuation length decreases for higher energies. In Fe however, the effective attenuation length increases for energies above the second threshold. This suggests that the interface band structure of Fe/Si may have a strong effect on the effective attenuation length.

Using BEEM (effective) attenuation lengths can be measured, but no spin-dependent information as spin-up or spin-down attenuation lengths of the hot electrons or holes can be quantified.

For obtaining magnetic and thus spin-dependent information BEEM is very suitable. A very important physical quantity that is used to determine spin-dependent properties is the magneto current. It is defined as:

$$MC = \frac{I_{C,P} - I_{C,AP}}{I_{C,AP}} \times 100\% \quad (13)$$

$I_{C,P}$ is the collector current when the two ferromagnetic layers in a spin valve are magnetically aligned parallel, $I_{C,AP}$ is the collector current for anti-parallel alignment. By applying a magnetic field parallel to the surface the magnetic orientation of the two ferromagnetic layers can be altered. The difference between $I_{C,P}$ and $I_{C,AP}$ is demonstrated in measurements on Au/NiFe/Cu/Co/GaAs(001) by Heer *et al.* [25] in Fig 17(a). The collector current measured on a fixed position as function of applied magnetic field is shown in Fig 17(b). First a field of -70 Oe was applied (red graph), forcing the ferromagnetic layers into a parallel alignment. The magnetic field is then swept to +70 Oe and back to -70 Oe (blue graph). A difference in the coercivity of NiFe and Co causes an anti-parallel alignment between $\sim \pm 20$ -45 Oe, and a parallel alignment only for higher applied magnetic fields. The anti-parallel alignment results into a lower collector current. In the given example the magneto current has a value of $MC \sim 600\%$ at room temperature.

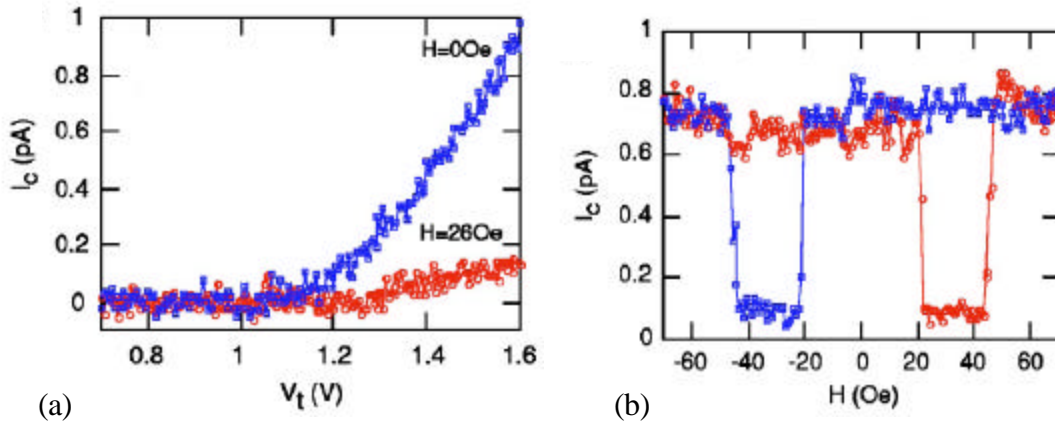


Fig 17. (a) BEEM spectra recorded on Au/NiFe/Cu/Co/GaAs(001) corresponding to parallel and anti-parallel alignment. (b) Collector current measured as function of magnetic field.

Figure is reproduced from [25].

The collector current in parallel ($I_{C,P}$) and anti-parallel ($I_{C,AP}$) alignment can be modeled using the following equations [26]:

$$I_{C,P} = I_0 (f_+ T_{o+} T_{i+}^* T_{o+}^* e^{-d_1/l_+} e^{-d_2/l_+} + f_- T_{o-} T_{i-}^* T_{o-}^* e^{-d_1/l_-} e^{-d_2/l_-}) \quad (14)$$

$$I_{C,AP} = I_0 (f_+ T_{o+} T_{i-}^* T_{o-}^* e^{-d_1/l_+} e^{-d_2/l_-} + f_- T_{o-} T_{i+}^* T_{o+}^* e^{-d_1/l_-} e^{-d_2/l_+}) \quad (15)$$

Here $f_{(-)}$ is the fraction of majority (minority) electrons in the initial tunneling current after transferring through the first ferromagnetic layer, $T_{(-)}$ is the effective majority (minority) attenuation length, $T_{0(i)+(-)}$ is the transmission coefficient out (into) a ferromagnetic layer for majority (minority) electrons. $d_{(2)}$ is the thickness of the first (second) ferromagnetic layer. The $*$ denotes the second ferromagnetic layer.

Using the spin valve construction with varying total thickness of the ferromagnetic layers and applying the BEMM technique, interesting properties of the spin-dependent attenuation length for hot electrons and polarizing effects at interfaces can be studied.

Rippard *et al.* did important studies on Co/Cu/Co trilayer films that are exemplary [26]. They measured $I_{C,P}$ and $I_{C,AP}$ were measured for as function of total Co thickness (2-60 Å) and tip voltage (1-2 V). They determined the energy dependent attenuation length and the polarizing effect of tunneling and transmission through the Co/Cu interface, see Fig 18.

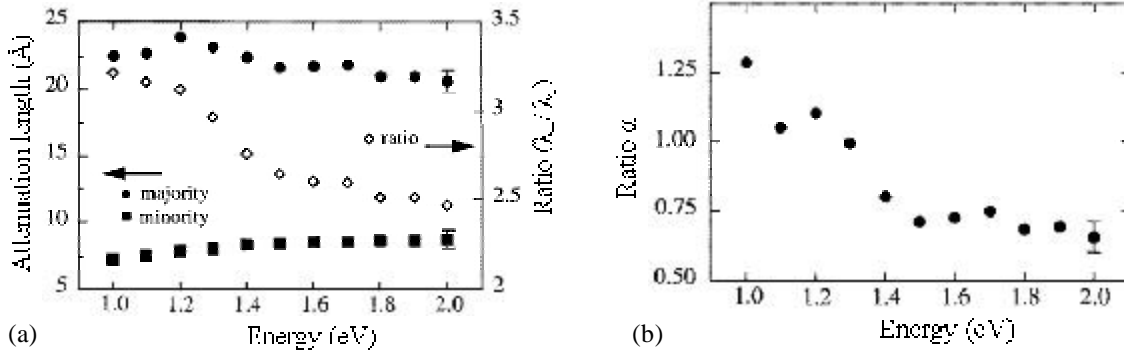


Fig 18. (a) Attenuation lengths for majority and minority electrons in Co and their ratio as function of electron injection energy. (b) Ratio (a) minority/majority electrons passing through first Co/Cu interface. Figure is reproduced from [26].

The attenuation length for minority electrons can be seen to increase (Fig 18(a)), this is contributed to a crossover from minority electrons propagating in the more localized d-band to propagating in the higher-velocity s-p band at increased energies [31]. The attenuation length for majority electrons remains relatively constant for energies below ~1.3 eV, but decreases for higher energies as the DOS in the d-band increases resulting in increased scattering [32].

It has been shown [27] that around E_F transmission of electrons through a Co/Cu interface is strongly spin-dependent and is stronger for majority electrons. A spin filtering effect can also be seen of energies above E_F , see Fig 18(b). For energies below ~1.2 eV more minority electrons are transmitted, for energies above ~1.3 eV more majority electrons. This is contributed to a decrease in the DOS for minority electrons due to the

d-band contribution. So for very thin (a few ?) Co layers this results in a minority-spin polarized beam below ~ 1.2 eV, for higher energies or thicker samples the transmitted beam is majority-spin polarized.

By using the spin-dependent attenuation lengths in Co, a polarizer-analyzer system can be created. Perella *et al.* used this to measure the effects of scattering on spin-dependent transport [28]. They used a Co/Cu/Al/Cu/Co/Au/Si(111) sample and measured $I_{C,P}$ and $I_{C,AP}$. As the spin-dependent scattering process at the Co/Cu interface and in Co are well known, the polarization out of the Cu/Al/Cu spacer layer can be determined. The polarization through the Al spacer is reduced by exposing it to oxygen, see Fig 19(a). At constant tip voltage, the polarization as function of collected current for the differently exposed spacer layers is shown in Fig 19(b). Increased oxygen exposure causes increased electron-electrons scattering, decreasing the collector current. Even though electron-electron scattering is spin conserving, it is found that the polarization decreases as additional unpolarized electrons are created through the creation of electron-hole pairs.

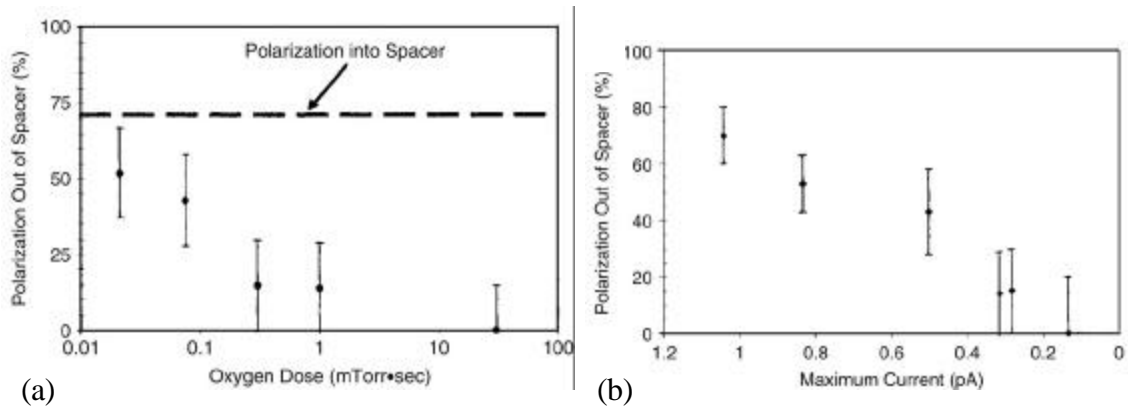


Fig 19. (a) The electron polarization exiting the spacer layer of Co/Cu/Al/Cu/Co/Cu/Au/Si(111) samples as function of the oxygen dose in the Al film. (b) The polarization exiting the spacer layer as a function of the maximum current at a tip voltage $V_T = -2$ V. Figure is reproduced from [28].

4.2 Hot holes

As hot electrons show (strong) loss of polarization when transferring through interfaces, it was of interest if this would also be the case for hot holes. Also a complete picture for non-equilibrium phenomena requires an understanding of spin-dependent behaviour of hot holes. Increased difficulty in the experimental technique arises however, especially due to low signal strengths.

Hot hole (effective) attenuation lengths can be determined as described earlier, by measuring the collector current for constant tip voltage and varying layer thickness. Banerjee *et al.* determined this way the energy dependent effective attenuation length for holes in Co [21], see Fig 20(a). The observed attenuation length of holes in Co ($\sim 6-10$ Å) is shorter than for hot majority electrons (~ 22 Å as seen in Fig 18(a), measured by [26]). As the spin resolved DOS of Co does not show any great fluctuations between majority and minority electrons in the energy range of 1-2 eV below E_F (see Fig 12), the increase

in the attenuation length cannot be explained by scattering, but must be contributed to a energy dependent propagation velocity. It is also demonstrated that the hole transmission of a $\text{Ni}_{81}\text{Fe}_{19}/\text{Au}/\text{Co}$ trilayer is clearly dependent on the magnetic alignment, see Fig 20(b). A magneto current $\text{MC}=130\%$ is shown, demonstrating the transmission of holes in both the ferromagnetic metals is spin-dependent. As this also cannot be explained by an asymmetry in the number of states to decay into for majority and minority holes, it is contributed to a difference in group velocity of holes with different spin.

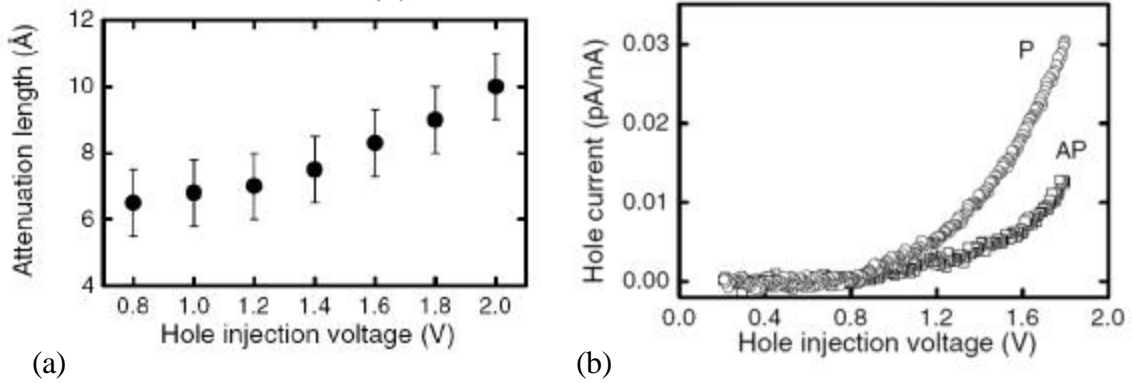


Fig 20. (a) Hole attenuation length in Co as function of hole injection voltage. (b) I_C measured as function of V_T for parallel and anti-parallel magnetic alignment in $\text{Au}/\text{Co}/\text{Au}/\text{Ni}_{81}\text{Fe}_{19}/\text{Au}/\text{Si}$.

Figure is reproduced from [21].

Low signal limits the exact determination of the attenuation length for majority and minority hot holes by this technique. The signal strength can be increased by operating BHMM in reverse mode, but the scattering mechanisms operating in this mode and the creation and transport of the scattered carriers and their influence on the collected current is an open question today.

Haq *et al.* performed measurements using R-BHMM on $\text{Co}/\text{Au}/\text{Ni}_{81}\text{Fe}_{19}$ trilayer structures [29]. A large magneto current was demonstrated, with values up to $\text{MC}=250\%$, see Fig 21(a). The positive value of MC is remarkable, as in the anti-parallel state more hot electron scattering occurs and therefore more electron-hole pairs are created. This indicates the position of scattering and the spin of the excited holes has to be taken into account. By varying the $\text{Ni}_{81}\text{Fe}_{19}$ thickness the effective attenuation length for different magnetic alignments can be determined, see Fig 21 (b). A clear sensitivity to the magnetic field is observed, but no strong energetic dependency. As the scattering processes that create the hot holes are not sufficiently modeled, it is however so far not possible to derive the exact energetic dependence of the majority and minority hot holes.

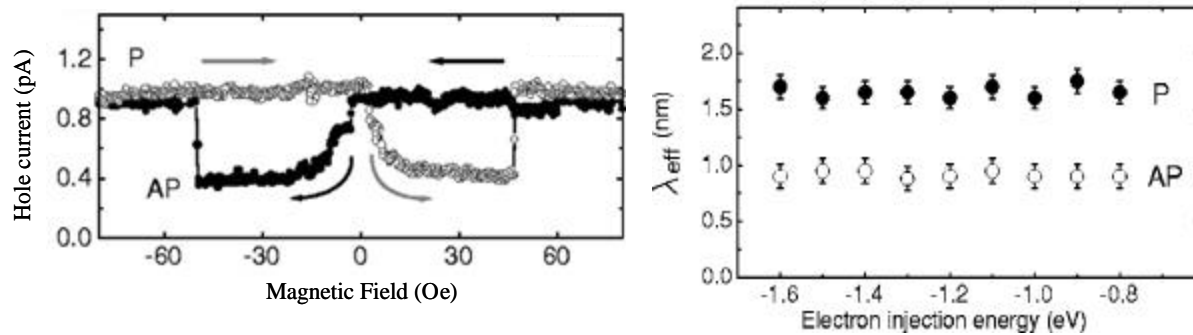


Fig 21. (a) hole current vs magnetic field for Au/Co/Au/Ni₈₁Fe₁₉/Au/p-Si. $I_T=4$ nA, $T=150$ K, $V_T= -1.6$ V.
 (b) Effective attenuation length in Ni₈₁Fe₁₉ for different alignments of Co and Ni₈₁Fe₁₉.
 Figure is reproduced from [29].

5 Nanoscale magnetic imaging

Because of the highly forward directed motion of the hot electrons, BEEM has proven to be a powerful imaging tool able to resolve atomic scale resolution.

The BEMM and R-BHMM techniques have also demonstrated to allow magnetic imaging with nanoscale resolution. R-BHMM is more preferable to use than BHMM as it leads to a higher collector current and thus better imaging.

A nice demonstration is by W.H. Rippard and R.A. Buhrmann who used BEMM to image Co/Cu/Co trilayer films while applying a magnetic field [30]. In Fig 22(a,b) it is shown how the domains change when the field is reduced from 30 Oe to 0 Oe in sputtered films. When comparing the change of the domains from parallel (white) to anti-parallel (black) on a smaller scale between sputtered (Fig 22(c)) and evaporated (Fig 22(d)) films it can be seen when taking cross-sections (Fig 22 (e,f)), that the domains changes on scales ~ 10 nm to several 100 nm. Also a clear difference in structure can be seen, probably indicating the sputtered film contains more defects.

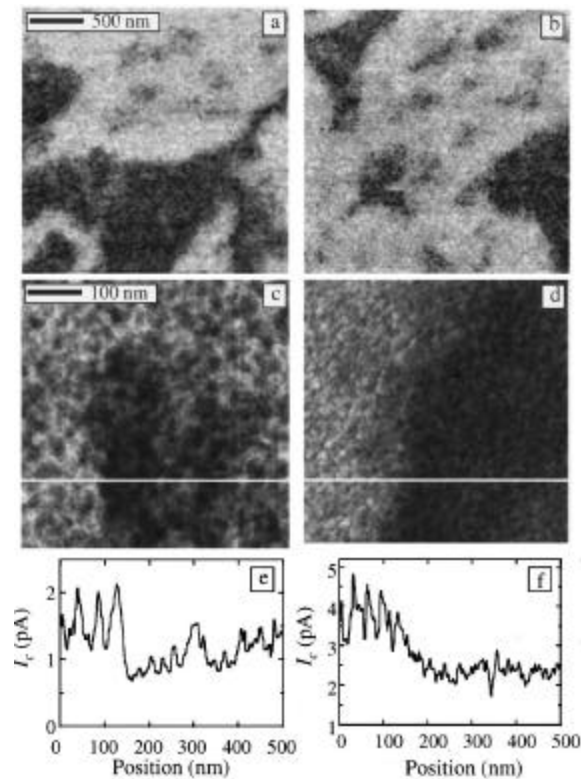


Fig 22. BEEM image of Au/Cu/Co/Cu/Co/Cu/Au/Si(111) structures at (a) $H = 30$ Oe and (b) $H = 0$ Oe. $500 \times 500 \text{ nm}^2$ BEMM images of similar (c) sputtered and (d) evaporated films. Cross sectional plots of the white lines in (c,d) are shown below their respective images in (e,f). Figure is reproduced from [30].

A nice demonstration of the magnetic resolution that is capable of being achieved using R-BHMM is given by Haq *et al.* [23]. The applied magnetic field was varied from +100 Oe to -100 Oe (Fig 23(a-f)) and clear domains of parallel (yellow) and anti-parallel (dark) alignment between Co and $\text{Ni}_{81}\text{Fe}_{19}$ can be seen. A 360° domain wall can clearly be seen in Fig 23(e) of which a cross-section is taken in Fig 23(g). An upper limit to the spatial resolution is provided by defining the distance over which the signal increases from 20% to 80% of the maximum value, in this case 28 nm. Presently even higher resolutions of 20 nm have been found.

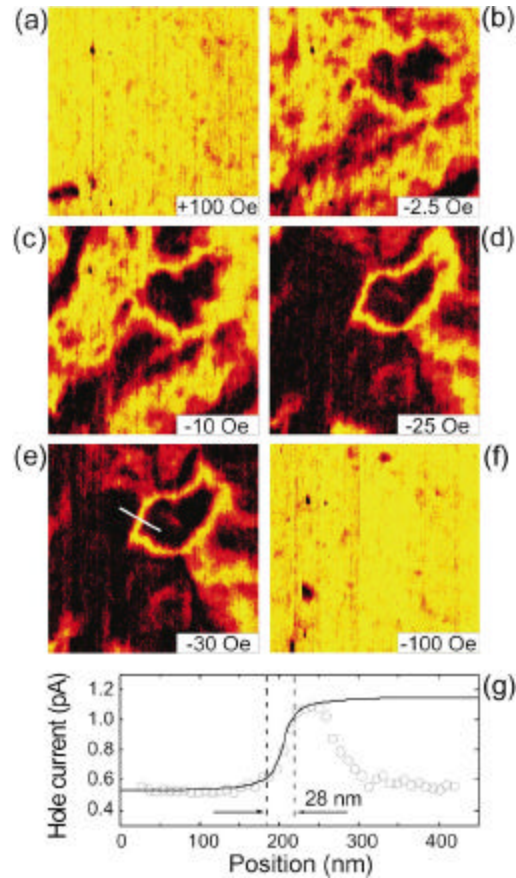


Fig 23. R-BHMM image of $2 \times 2 \mu\text{m}^2$ Au/Co/Au/ $\text{Ni}_{81}\text{Fe}_{19}$ /Au/p-Si sample for (a-f) varying magnetic fields. (g) Cross section along white line in (e). $V_T = -1.6$ V, $I_T = 3$ nA, $T = 150$ K. Figure is reproduced from [23].

Conclusions

It is inconclusive whether the resolutions that have been achieved using BEEM and RBHMM (~ 10 nm for BEEM [23], ~ 20 nm for RBHM), can be further enhanced.

A simplistic approach to determining the resolution is by using Equation 5 and estimate the resolution R by $R \sim d \cdot \tan(\theta_c)$, with d the thickness of the metal layer stack. In experiments where an Au/Si Schottky barrier is used, $V_0 \sim 0.8$ V (for electrons) and $V_0 \sim 0.3$ V (for holes). In most metals the Fermi-energy $E_F \sim 5$ eV and typically $V_T \sim 0.5$ V above V_0 to obtain a good signal. The effective masses of electrons and holes depends on the used semiconductor substrate and orientation, for example for Si(100) $m^* = 0.98 m_0$ (for electrons) and $m^* = 0.49 m_0$ (for holes) [33]. Assuming the mass of electrons and holes in metals $m_0 = m_0$, for BEEM this results in a lateral resolution $R \sim 30\%$ of the thickness of the metal layer stack and for BHMM $R \sim 24\%$. For a typical metal layer stack of thickness $d = 20$ nm this would indicate that a resolution down to $\sim 4-6$ nm should be achievable and even better resolution for thinner stacks or by using semiconductors with a smaller electron or hole effective mass.

Clearly BEEM and the techniques related to it hold great promise of achieving even smaller resolutions than up to date have been achieved. It is therefore a promising tool to expand our understanding how magnetic structures and interfaces behave on the nano-scale.

Modelling will have to be done to better understand the physical transport mechanisms and the transport of scattered carriers, as occur for example in RBHMM. The field of ballistic hole magnetic transport is still largely undiscovered, but for this purpose the technique is very encouraging. BEEM and related techniques therefore holds great promise for revealing more understanding about spin-dependent transport.

Acknowledgements

I would like to thank dr. Tamalika Banerjee for all her help.

References

- [1] W. J. Kaiser, L. D. Bell, Phys. Rev. Lett. **60** (1988) 1406
- [2] M.H. Hecht, L.P. Bell, W.J. Kaiser, L.C. Davis, Phys Rev. B **42** (1990) 7663:60
- [3] L.D. Bell, W.J. Kaiser, Annu. Rev. Mater. Sci. **26** (1996) 189
- [4] A. Davies, H.G. Craighead, Appl. Phys. Lett. **64** (1994) 2833
- [5] LD Bell, WJ Kaiser, Phys. Rev. Lett. **61**, (1988) 2368
- [6] R. Ludeke, M. Prietsch, J. Vac. Sci. Technol. A **9** (1991) 885
- [7] J.G.Simmons, J Appl. Phys. **35**, 2655 (1964)
- [8] E.L. Wolf, Principles of Electron Tunneling spectroscopy (Oxford, New York, 1985), chap. 2
- [9] M. Prietsch /Physics Reports **253** (1995) 163-233
- [10] E Haq PhD thesis, 2005, University of Twente, The Netherlands
- [11] DJ BenDaniel, CB Duke, Phys. Rev. **152**, (1966) 683
- [12] D.L. Smith, M. Kozhevnikov, E.Y. Lee, V. Narayanamurti, Phys. Rev. B **61** (2000) 13914
- [13] M. Prietsch, Phys. Rep. **253** (1995) 163
- [14] D. K. Guthrie *et al.*, Phys. Rev. B **54**, (1996) 16972-16983
- [15] Bobisch *et al.*, PRL **102**, (2009) 136807
- [16] H. Siringhaus, E.Y. Lee, H. van Kanel, Phys, Rev. Lett. **74** (1995) 3999
- [17] M.N. Baibich *et al.*, Phys. Rev. Lett. **64** (1988) 2472-2475
- [18] G. Binasch, P. Grünberg, F. Saurenbach, W. Zinn, Phys. Rev. B **39** (1989): 4828–4830
- [19] C. Chappert *et al.*, Nature Materials, **6**, (nov 2007) 813-823
- [20] W.H. Rippard, R.A. Buhrman, Appl. Phys. Lett. **75** (1999) 1001
- [21] T. Banerjee *et al.*, Phys. Rev. Lett **94**, (2005) 027204
- [22] B Engel *et al.*, IEEE Trans. Magn. **41**, (2005), 132-136
- [23] E. Haq *et al.*, Appl. Phys. Lett **86** (2005) 082502
- [24] A.J. Stollenwerk *et al.*, Phys. Rev. B **74** (2006) 155328
- [25] R Heer *et al.*, Appl. Phys Lett. **85** (2004) 4388
- [26] W.H. Rippard, R.A. Buhrman, Phys. Rev. Lett. **84** (2000) 971
- [27] M.D. Stiles, J Appl. Phys. **79** (1996) 5805-5810
- [28] AC Perrella *et al.*, j appl. Phys **98** (2005) 093717
- [29] E. Haq *et al.*, Appl. Phys. Lett. **88** (2006) 242501
- [30] W. H. Rippard, R. A. Buhrman, J. Appl. Phys. **87** (2000) 6490
- [31] E. Yu, Tsymbal and D.G. Pettifor, Phys. Rev. B **54** (1996) 15314
- [32] E. Zarate, P. Apell and P.M. Echenique, Phys. Rev. B **60** (1999) 2326
- [33] <http://www.ioffe.rssi.ru/SVA/NSM/Semicond/Si/bandstr.html#Masses>